Journal of Nuclear Materials 533 (2020) 152105

Contents lists available at ScienceDirect

Journal of Nuclear Materials

journal homepage: www.elsevier.com/locate/jnucmat

The effect of Zr on precipitation in oxide dispersion strengthened FeCrAl alloys☆

Caleb P. Massey [a, *], Philip D. Edmondson [a], Kinga A. Unocic [a], Ying Yang [a], Sebastien N. Dryepondt [a], Anoop Kini [b], Baptiste Gault [b], Kurt A. Terrani [a], Steven J. Zinkle [a, c]

[a] Oak Ridge National Laboratory, Oak Ridge, 37831, TN, USA
[b] Max-Planck-Institut Für Eisenforschung GmbH, Düsseldorf, Germany
[c] University of Tennessee, Knoxville, 37996, TN, USA

GRAPHICAL ABSTRACT

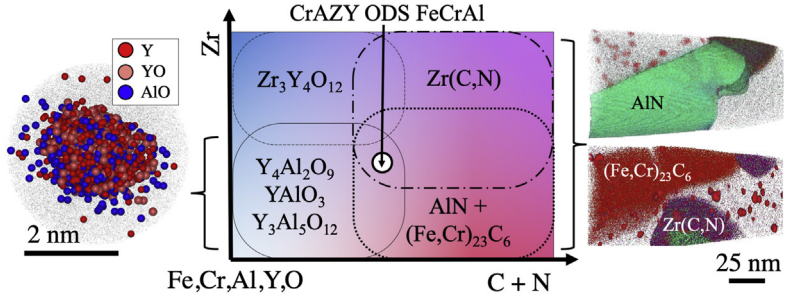

ARTICLE INFO

Article history:
Received 29 January 2020
Received in revised form
6 March 2020
Accepted 7 March 2020
Available online xxx

Keywords:
Atom probe tomography
Oxide dispersion strengthened (ODS) alloy
Precipitation
Electron microscopy

ABSTRACT

Oxide dispersion strengthened (ODS) FeCrAl alloys are promising candidate materials for advanced nuclear reactor applications requiring high-temperature strength, corrosion resistance, and irradiation tolerance. As these alloys have increased in compositional complexity through attempts to use highly reactive elements such as Zr to refine particle sizes and optimize nanoprecipitate dispersion characteristics, much debate has ensued as to the effects of these alloying element additions on alloy properties. In an attempt to reconcile differences in nanoprecipitate distributions reported in the literature over the past decade, a detailed investigation of a recently developed ODS FeCrAl alloy with nominal composition Fe−10Cr-6.1Al-0.3Zr+0.3Y_2O_3 is presented using a combination of atom probe tomography (APT), scanning/transmission electron microscopy (S/TEM), and computational thermodynamics modeling. It is illustrated that based on the amount of Zr available in the lattice, Zr competes with Al and Cr to form carbides and nitrides as opposed to oxygen-rich precipitates. This alloy system has a high number density (>10^{23} m^{-3}) of ~2–4 nm diameter (Y,Al,O)-rich nanoprecipitates, but it is shown that due to the compositional spread and unknown partitioning of Al between the matrix and precipitates, significant challenges still exist for quantifying the exact compositions of these precipitates using APT. However, the noted compositional spread is supported by identified complex oxides yttrium aluminum monoclinic

☆ This manuscript has been authored by UT-Battelle, LLC, under contract DE-AC05-00OR22725 with the US Department of Energy (DOE). The US government retains and the publisher, by accepting the article for publication, acknowledges that the US government retains a nonexclusive, paid-up, irrevocable, worldwide license to publish or reproduce the published form of this manuscript, or allow others to do so, for US government purposes. DOE will provide public access to these results of federally sponsored research in accordance with the DOE Public Access Plan (http://energy.gov/downloads/doe-public-access-plan).

* Corresponding author.
E-mail address: masseycp@ornl.gov (C.P. Massey).

https://doi.org/10.1016/j.jnucmat.2020.152105

(YAM) and yttrium aluminum garnet (YAG) using S/TEM. As a result of these findings, researchers developing ODS FeCrAl with reactive element additions must pay careful attention to C and N impurities when optimizing reactive element additions.

1. Introduction

In the search for advanced materials capable of withstanding high temperatures and corrosive environments while retaining mechanical integrity, oxide dispersion strengthened (ODS) Fe-based alloys have proven to be promising candidates for a variety of applications. First developed for gas turbine, furnace, and space applications requiring hot-gas corrosion resistance and enhanced creep strength, legacy ODS Fe-based alloys with Cr and Al additions (ODS FeCrAl) alloys MA956 and PM2000 received much attention for these purposes [1]. The exceptional oxidation resistance of the FeCrAl alloy stems from a passive alumina layer that forms in air and steam environments [2,3]. Coupled with a dispersion of complex oxides throughout the material that impede dislocation motion and pin grain boundaries, these alloys exhibited enhanced creep-rupture strengths in comparison to wrought FeCrAl variants [1].

In comparison to these environments, no application is more extreme than those proposed for advanced nuclear reactor designs. With operating temperatures of advanced fission and fusion reactor concepts in the range of 300−1000 °C and with irradiation doses expected to climb as high as 200 dpa for some designs, these alloys would not only require retention of their high-temperature corrosion and mechanical properties, but they would also need to mitigate many irradiation-induced degradation phenomena associated with these temperature/dose regimes [4]. In addition, with many currently operating light water reactors nearing the end of their licensing lifetimes, there is increased interest in advanced materials that can extend reactor lifetimes while simultaneously increasing safety margins in the event of an accident scenario [5,6].

Consequently, ODS alloys have received renewed interest for a variety of nuclear reactor applications. In the case of existing light water reactors, lower-Cr (10−12 wt%) ODS FeCrAl variants have been under development (1) to provide enhanced oxidation resistance and mechanical integrity under postulated loss-of-coolant accident scenarios [7,8], (2) to mitigate deleterious embrittlement stemming from Cr-rich α' -precipitation in normal operating temperature regimes [9], and (3) to reduce irradiation-induced hardening by optimizing nanoprecipitate distributions to provide a high-number density of sinks for irradiation defects [4]. For fusion blanket applications, the addition of Al has been shown to greatly enhance corrosion resistance in Pb−Li environments [10], and for other advanced fission reactor concepts, ODS Fe-based alloys have exhibited exceptional resistance to void swelling, even at high irradiation doses [11,12].

However, nanoprecipitates in legacy ODS FeCrAl alloys MA956 and PM2000 are not ideal for nuclear applications requiring high sink strength. In comparison to popular ODS FeCr alloys MA957 and 14YWT without Al-addition, MA956 and PM2000 have nanoprecipitate distributions that are much coarser and lower in number density. This is because the addition of Al to the ODS FeCr alloy shifts the types of preferentially nucleated precipitates from highly stable (Y,Ti,O)-rich nanoprecipitates to (Y,Al,O)-rich precipitates that exhibit less resistance to coarsening at the high temperatures typically used for material fabrication [13−15]. As a result, recent studies have focused on the development of ODS FeCrAl-specific thermomechanical processing parameters to maximize nanoprecipitate populations and to optimize mechanical properties [16−18].

Using a different approach, some researchers have added highly reactive elements to fabricated ODS FeCrAl alloys to shift the types of nanoprecipitates that nucleate from (Y,Al,O)-rich precipitates to more stable complex oxides. Additions of Zr and Hf have been demonstrated to reduce the average nanoprecipitate diameter from 6.7 nm to 4.8 and 4.3 nm, respectively [18−20]. Along with the decrease in precipitate diameter, the researchers also indicate that the precipitates shift from (Y,Al,O)-rich compositions to either $Y_4Zr_3O_{12}$ or $Y_2Hf_2O_7$. These results differ from recent work by Unocic et al., who developed low-Cr ODS FeCrAl alloys with similar additions of Zr, where instead of seeing a competition between Al and Zr for nucleation and growth of the smallest oxide precipitates, they found that Zr was primarily associated with Zr(C,N)-rich precipitates [21]. However, in Unocic's prior work, the alloy investigated was unique in that the Zr and Y additions were added in the form of ZrO_2 and Y_2O_3 ball milled with Fe−12Cr-5.6Al gas atomized powder. The authors in this previous work acknowledged that since the Zr alloying element was added by ball milling ZrO_2 into the microstructure, it is possible that Zr was not sufficiently incorporated homogeneously throughout the microstructure in a manner that allowed for a direct comparison with other studies where Zr was added through a gas-atomization process into the host powder. The uncertainties with respect to the effective dispersion of Zr throughout the microstructure, coupled with the extremely high oxygen content of Unocic's alloy (1920 parts per million by weight) may have shifted the types of precipitates such that a direct comparison with prior work on Zr addition may not be applicable.

Because the types of nanoprecipitates that nucleate within nuclear-grade ODS FeCrAl are of crucial importance to establishing optimized thermomechanical processing parameters since the coarsening rates have been shown to differ between (Y,Zr,O)-rich and (Y,Al,O)-rich nanoprecipitates [14], and also due to potential differences in nanoprecipitate stability under irradiation as a function of precipitate composition, a comprehensive investigation of the effect of highly reactive elements such as Zr was undertaken. Using an alloy with Zr already gas-atomized into the ODS FeCrAl powder, this work aims to identify the effect of Zr on the formation of the smallest nanoprecipitates in a series of ODS FeCrAl alloys, thereby resolving the discrepancies between prior studies and establishing a framework for optimizing alloy irradiation resistance and mechanical response. Through a comprehensive comparison of a recently fabricated ODS Fe-based alloy with nominal composition Fe−10Cr-6.1Al-0.3Zr+0.3Y_2O_3, atom probe tomography (APT) is coupled with electron microscopy to characterize the dispersions and compositions of various precipitates within the microstructure in both powder and consolidated form. This new CrAZY alloy, with Zr added directly into the FeCrAl powder using gas atomization, provides a more realistic assessment as to the role of Zr in precipitation. By combining the atomic-scale microscopy methods utilized in this work, new insights in accurate compositional measurements for the smallest nanoprecipitates are presented. Coupled with thermodynamic calculations using the ThermoCalc

software, it is shown that researchers developing ODS FeCrAl with reactive element additions must pay careful attention to C and N impurities when optimizing reactive element additions.

2. Materials and methods

2.1. Specimen preparation

To produce the low-Cr ODS FeCrAl alloys containing Fe, Cr, Al, Zr, and Y (designated CrAZY alloys in this work), the mechanical alloying powder metallurgical route was taken. Gas atomized Fe−10Cr-6.1Al-0.3Zr (wt.%) powder from ATI Powder Metals, with an average particle size ranging from 44 to 149 μm diameter, was mixed with nanocrystalline yttria (25−50 nm in crystallite size) acquired from Alfa Aesar and ball-milled under Ar atmosphere for 40 h using low-C steel milling media. This CrAZY ODS FeCrAl alloy has only 10 wt% Cr and has Zr added directly into the initial powder through a gas-atomization process, which is markedly different than previous 1 st Generation ODS FeCrAl alloys such as 125YZ previously reported in literature [21]. Milling was performed using a CM08 Zoz Simoloyer ball mill with a chamber large enough to hold 1 kg of powder charge. During the alloying step, 350 rpm/600 rpm rotational speeds were used with a ball-to-powder ratio of 10:1.

After mechanical alloying, ~20 g of powder extracted from the CM08 unit was encapsulated in an evacuated (10^{-4} Torr) quartz vial and annealed at 1000 °C for 1 h, resulting in an annealed powder specimen designated as ZY10C60. This specimen was previously investigated using APT for the quantification of precipitate coarsening kinetics, but detailed investigations of nanoprecipitate dispersions and compositions have not yet been undertaken for this annealed powder [16]. In addition, ~600 g of milled powder from the same milling batch was packed into a mild steel extrusion can (4.83 cm OD), degassed at 300 °C for 24 h, and extruded at 1000 °C after annealing for 1 h in the same manner as the ex-situ annealed powder specimen. For the extrusion, a circular die with diameter 2.22 cm, was used to create cylindrical bar stock. This specimen is designated as 4H10C to remain consistent in nomenclature with prior work on CrAZY ODS alloy extrusions [17]. A visual representation of the specimen fabrication process is illustrated in Fig. 1. The annealed powder specimen (ZY10C60) and the extruded alloy (4H10C), in addition to the as-received gas atomized FeCrAlZr powder and milling media, were analyzed using inductively coupled plasma optical emission spectroscopy (ICP-OES), and the chemical compositions of each specimen are presented in Table 1.

2.2. Data collection and analysis

The primary means of investigating the nanoprecipitate distributions in these CrAZY specimens included APT and scanning transmission electron microscopy (S/TEM) methods. APT specimens were prepared at the Max-Planck-Institut for Eisenforschung (MPIE) in Düsseldorf, Germany, for both the annealed powder and the extruded alloy using a FEI Helios 600 focused ion beam (FIB). Details of the FIB liftout technique used for APT specimen preparation can be found in Miller's 2007 paper [22]. APT needle shaping/annular milling was performed using 30 kV Ga ions, while final sharpening was performed using 5 kV ions to minimize ion implantation into each sample. Operating in laser mode with a laser pulse energy of 32 pJ and a pulse frequency of 200 kHz, a Cameca LEAP 5000 XR local electrode atom probe (LEAP) at MPIE was used to collect the APT data. The target detection rate was set to 5 ions per 1000 laser pulses to minimize the number of multiple ions detected during the same laser pulse event. At least two specimens were prepared from both the annealed and extruded powder. Although some heterogeneity may be expected due to the nature by which these alloys were fabricated, the precipitate distributions in all of the observed control volumes were highly homogeneous, with only one precipitate free zone observed in these samples. This way, a sufficiently high number of nanoprecipitates could be collected for adequate sample statistics.

For data analysis, Cameca's Integrated Visualization & Analysis Software (IVAS) package (version 3.6.8) was used to identify body-centered-cubic (BCC) poles within each sample for accurate sample reconstruction [23−26]. Each range file was imported into Matlab, and each peak in the mass-to-charge ratio spectrum was binned to full-width tenth-maximum (FWTM) conditions to ensure consistent sample-to-sample compositional measurements. Afterwards, the bulk composition of each specimen was calculated using peak decomposition algorithms built into the IVAS software package [27,28]. This was needed due to several mass-to-charge ratio peak overlaps for various ions such as at 27 Da ($^{27}Al^{+1}$, $^{54}Cr^{+2}$, $^{54}Fe^{+2}$), 54 Da ($^{54}Cr^{+1}$, $^{54}Fe^{+1}$), and 32 Da ($^{16}O_2^{+1}$, $^{96}Zr^{+3}$). To identify the smallest populations of nanoprecipitates in this work, the maximum separation method was applied that uses iteratively determined parameters (1) N_{min}, the minimum number of solute atoms associated with a cluster, and (2) d_{max}, the maximum diameter defining the cluster [23,25,26]. For larger precipitates, isoconcentration surfaces were used instead of the maximum separation methodology.

For accurate compositional measurements of the smallest nanoprecipitates identified using the maximum separation method, two separate methodologies were used. First, the as-exported cluster

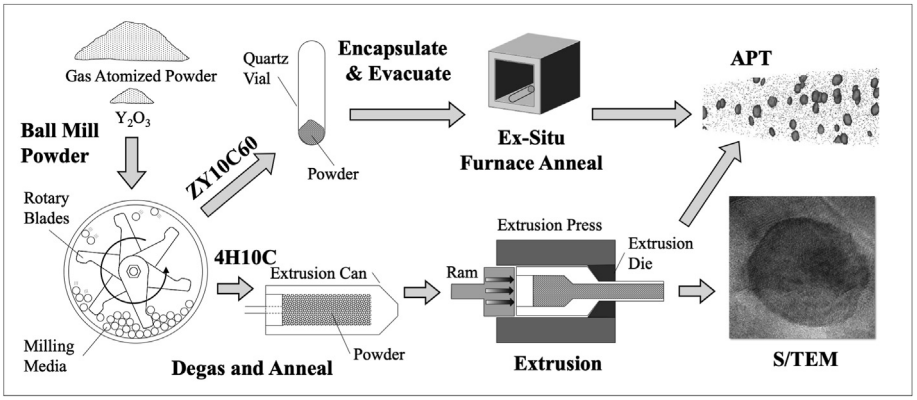

Fig. 1. Process diagram for specimen preparation and evaluation.

Table 1
Chemical compositions of powders (at. %) and alloys provided by DIRATS using ICP-OES. As governed by the test method, the error of each value is within 2% of the mean value reported in the table.

Sample	Form	Mill	Fe	Cr	Al	Zr	Y	O	C	N
Milling media	5 mm steel ball	n/a	93.40	1.62	0.02	0.00	0.00	0.00	4.17	0.01
Gas atomized powder	Powder	n/a	77.40	10.00	12.34	0.17	0.00	0.06	0.02	0.01
ZY10C60 [16]	Annealed powder	CM08	77.42	9.73	11.78	0.15	0.13	0.43	0.25	0.04
4H10C	Extruded alloy	CM08	78.00	9.55	11.33	0.15	0.12	0.38	0.26	0.12

analysis file is not corrected for the peak-overlaps previously mentioned. Edmondson et al. [29] have developed a methodology that compares the ratio of the as-measured bulk composition to the bulk composition exported from the cluster analysis file and establishes correction factors for each element that are then multiplied to the matrix and cluster compositions to correct for peak-overlaps. The resulting cluster compositions are referred to in this work as *uncorrected* cluster compositions since no further corrections are made for spatial overlaps associated with trajectory aberration overlaps.

The second correction involves consideration of differences in the evaporation rates of the precipitates and the surrounding matrix. It is well known in the literature that high matrix concentrations such as Fe and Cr are erroneously measured in precipitate compositions due to trajectory aberrations arising from these evaporation field differences [30,31]. For ODS FeCr alloys, multiple methods for subtracting these matrix-associated elements have been proposed. Noting that no Fe should exist in the smallest (Y,Ti,O)-rich nanoprecipitates in these ODS FeCr alloys, Williams et al. [32] have previously subtracted all of the Fe out of each precipitate and have correspondingly subtracted the remainder of the matrix elements in proportion to the measured matrix composition. Using a more robust approach, Hatzoglou et al. [33] have developed a chemical composition correction (CCC) model that takes increased atomic point densities in each precipitate into consideration, as well as differences in precipitate shape as a function of local magnification effects to correct compositions for each individual precipitate. For the nanoscale precipitates in this work, discussions regarding corrections for spatial overlaps will be framed with respect to this newly developed CCC model.

STEM specimens were prepared at the Low Activation Materials Development and Analysis (LAMDA) Laboratory at Oak Ridge National Laboratory (ORNL) [34] using a FEI Quanta 3D dual-beam FIB. 30 kV Ga ions were used for the initial liftout and thinning steps, while 2 kV Ga ions were used for final thinning to minimize ion beam damage to the STEM foils. To image the smallest nanoscale precipitates using S/TEM, an aberration-corrected JEOL 2200FS STEM was used; it was operated at 200 kV and was equipped with a CEOS GmbH corrector on the probe-forming lenses. Simultaneous bright-field and high-angle annular dark-field (HAADF) STEM imaging was acquired. For imaging, the convergence semi-angle was 26.5 mrad with an inner and outer 110 mrad and 470 mrad collection semi-angle for the HAADF STEM detector. The beam current was nominally 150 pA. A fast Fourier transform (FFT) was generated from the HR-STEM images, and d-spacing was measured based on present reflections using digital micrograph software. For S/TEM imaging with elemental analysis, a FEI (now ThermoFischer) Talos F200X S/TEM operating at 200 keV was used. The instrument combines high resolution imaging with a large solid-angle (0.9 srad) windowless energy dispersive x-ray spectroscopy detector. Here, imaging and elemental mapping were conducted using a probe current of ~1 nA and a probe size of approximately 1 nm at FWHM. Spectrum images were recorded over a 1024 $\times$ 1024 pixel region and collected and analyzed using Bruker Esprit software (v1.9) [35,36]. Multivariate statistical analysis (MVSA) was performed using Sandia National Laboratory's AXSIA code, with all the data presented having undergone 2 $\times$ 2 spatial, and 2x spectral binning [37]. Energy electron loss spectroscopy (EELS) was performed on a 300 kV aberration-corrected STEM/EELS FEI Titan. For general microstructure examination of the annealed powder and the extruded alloy, a Hitachi 4800 field emission scanning electron microscope (SEM) was used with an accelerating voltage of 15 kV.

3. Results

3.1. Specimen compositions and microstructure

The ICP-OES measured compositions of the specimens investigated in this work are listed in Table 1. The as-received gas-atomized FeCrAlZr powder is quite pure, with impurity contents in the tens of parts per million by weight of C, N, and O. After mechanically alloying and either annealing or extrusion, the C content increases by two orders of magnitude, which is expected due to the higher carbon content of the milling media that continually impacts the powder during the mechanical alloying stage. Similarly, the N and O contents also increase after the ball-milling step. The increase of O content arises from (1) the addition of yttria to the gas-atomized powder and (2) potential air-ingress into the milling chamber backfilled with Ar gas, whereas the increase in N content is attributed to air ingress during milling. There is a noted difference in measured N content when comparing the annealed powder and the extruded alloy. Since the exact same powder was used for both the powder anneal and the subsequent extrusion, the N content would be expected to be the same for both specimens. Since only 10 g of each sample was used for the ICP-OES chemical analysis, this difference might be attributed to inhomogeneous distribution of this impurity element throughout the as-milled powder.

The microstructures of the annealed CrAZY powder (ZY10C60) and the extruded alloy (4H10C) are shown in Fig. 2. It is readily apparent that significant differences exist in the grain structures of both samples. For the powder, the high stored energy within the powder specimen after mechanical alloying has resulted in abnormal grain growth mechanisms during the annealing step. This type of microstructure in ball-milled and annealed ODS powder has extensively been investigated by Sallez et al. [38], where a combination of the very fine grain structure after ball milling and an associated high dislocation density promote primary recrystallization when the temperature exceeds ~800 °C during annealing. Since the nucleation and growth of nanoprecipitates in both ODS FeCr and ODS FeCrAl alloys have been shown to occur at temperatures as low as 600 °C [16,39], the driving forces for this abnormal grain growth mechanism are accepted to be much higher than the Zener pinning of grain boundaries by nanoprecipitates within the microstructure, which explains the bi-modal grain structure of the powder. One important point regarding this bi-modal grain size is that in the previous study on the same annealed CrAZY powder, the nanoprecipitate distributions in both the fine- and coarse-grained regions appear identical [16]. As a

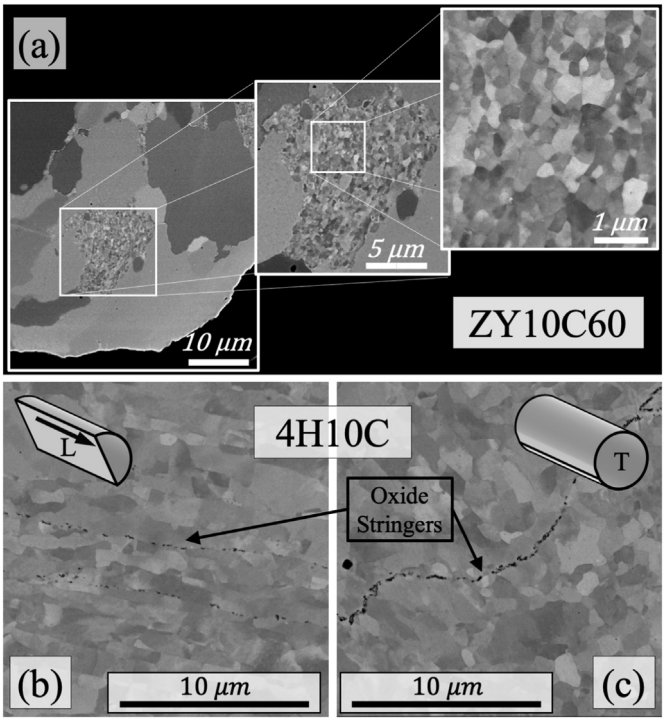

Fig. 2. SEM-BSE images of the (a) grain structure of the as-annealed ZY10C60 CrAZY powder after 60 min at 1000 °C, as well as (b) longitudinal "L" and (c) transverse "T" orientations for the as-extruded 4H10C sample consolidated after annealing for 60 min at 1000 °C. Also shown are oxide stringers oriented parallel to the extrusion direction.

result, direct comparisons of precipitate distributions between the annealed powder and the extruded alloy are possible.

Fortunately, the significant deformation associated with the subsequent extrusion step is sufficient to refine the bi-modal grain structure to a more unimodal structure, with some associated grain texture in the as-extruded microstructure. In the as-extruded specimen 4H10C, the average grain size in the longitudinal "L" orientation parallel to the extrusion direction was 755 ± 22 nm, while in the transverse "T" orientation perpendicular to the extrusion axis the grain size measured 678 ± 23 nm, with errors reported as the standard error of the mean. The resulting grain aspect ratio is 1.11, showing minimal grain elongation in the extrusion direction. Also noted in the as-extruded condition are stringers of precipitates, which are aligned in the extrusion direction as identified in Fig. 2. These precipitates have been noted in previous extruded ODS FeCrAl alloys [10] and are believed to be Al_2O_3 oxides that have resulted from the fracturing of a thin-alumina oxide layer on prior particle surfaces during the extrusion stage.

3.2. CrAZY nanoprecipitate distributions

A variety of different precipitate populations exist in both the CrAZY annealed powder and the as-extruded alloy. APT control volumes for both samples shown in Fig. 3 indicate identical precipitate dispersions and characteristics. Two different populations of precipitates exist in these control volumes. A dispersion of red precipitates highlighted using Y-, YO-, and AlO-rich isoconcentration surfaces comprises the finest and most integral nanoprecipitate population, as these precipitates serve as the primary obstacles for dislocation motion and as sinks for irradiation defects. In addition, coarser precipitates enriched primarily in Zr are highlighted in purple. To more effectively show the elemental segregations in each precipitate population, Fig. 4 depicts the atom maps of different atomic species within the 4H10C control volume previously shown in Fig. 3. The Y, YO, AlO, and O ionic species are clearly associated with the smallest nanoprecipitate population, while the larger precipitates appear to be enriched primarily in Zr and C.

There is a high number density of nanoprecipitates within both the annealed CrAZY powder and the extruded alloy. Although the number of nanoprecipitates varies somewhat between the two specimens, their number densities exceed 10^{23} m^{-3}, which is highly competitive with model ODS FeCr alloys 14YWT and MA957 that have been designed specifically for maximizing irradiation resistance through a high sink-strength approach [40–42]. In addition to the precipitate number densities (N_p), Table 2 includes the volume fraction occupied by the smallest precipitates (measured to be f~1%) and the average precipitate radius (R_s). Although previous APT studies have sometimes used the atomic count method to estimate nanoprecipitate radius (which uses the total number of ions within each precipitate and an assumed atomic density to estimate an equivalent spherical radius) this method is highly influenced by extra atoms erroneously measured in the precipitate due to trajectory aberrations [43–45]. Miller has previously shown that the spherical equivalent Guinier radius (R_s, defined as $\sqrt{5/3}$ multiplied by the measured radius of gyration of the precipitate) more accurately represents ODS FeCr nanoprecipitates measured using electron microscopy methods [46]. Consequently, this work reports the Guinier radius, as it is less prone to errors from APT artifacts. The radii measured in both samples are highly consistent between ZY10C60 and 4H10C.

APT results for the bulk compositions of both ZY10C60 and 4H10C are listed in Table 2, in addition to the matrix and uncorrected (Y,Al,O)-rich nanoprecipitate compositions. In comparison to the chemical analysis results presented in Table 1, the bulk compositions are quite accurate in terms of the primary Fe, Cr, and Al elements within the material. The corresponding matrix compositions are also comparable, aside from the reduction in Y content due to its segregation to the precipitates. With respect to the precipitate compositions, a significant amount of Fe and Cr is measured

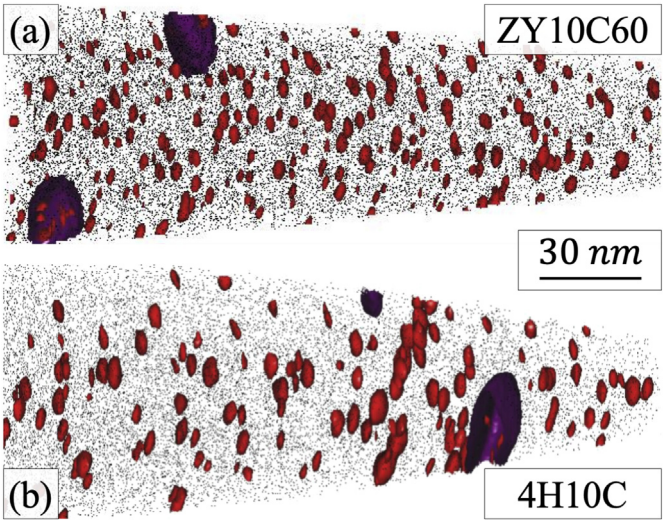

Fig. 3. APT control volumes for CrAZY (a) powder ZY10C60 annealed for 1 h at 1000 °C and (b) alloy 4H10C annealed for 1 h at 1000 °C followed by extrusion. Depicted are red 1.5 at.% (Y,Al,O) isoconcentration surfaces and purple 10 at.% Zr isoconcentration surfaces atop 0.1% of black Fe matrix atoms. (For interpretation of the references to color in this figure legend, the reader is referred to the Web version of this article.)

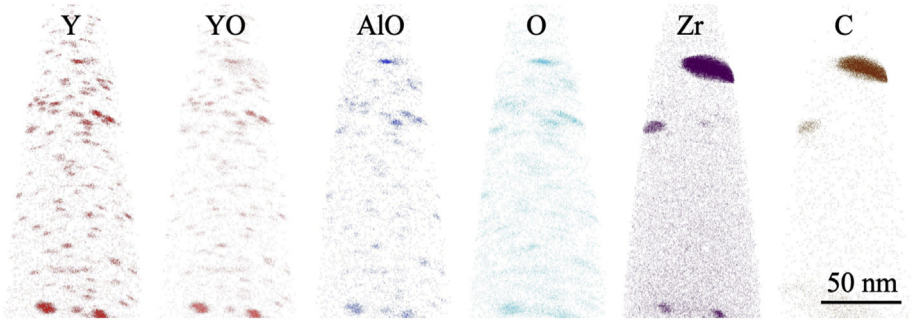

Fig. 4. Atom maps for various single ion and molecular ion species of interest in 4H10C extruded alloy.

Table 2
APT Results for bulk, matrix, and (uncorrected) precipitate compositions reported in atomic percent for the annealed ZY10C60 powder and 4H10C extruded alloy. Errors in precipitate sizes, number densities, and volume fractions are reported as the standard deviation of the mean for the measured sample distributions. Means and errors are computed based on the average of two different APT specimens for each sample, respectively.

	ZY10C60			4H10C		
	R_s [nm]		1.1 ± 0.3	**R_s [nm]**		1.1 ± 0.5
	N_p x10^{23} [m^{-3}]		5.0 ± 0.4	**N_p x10^{23} [m^{-3}]**		1.7 ± 0.2
	f [%]		1.7 ± 0.1	**f [%]**		0.8 ± 0.1
Element	**Prec.**	**Matrix**	**Bulk**	**Prec.**	**Matrix**	**Bulk**
Fe	64.64 ± 7.82	78.39 ± 0.42	78.26 ± 0.51	56.32 ± 13.10	78.78 ± 0.23	78.68 ± 0.27
Cr	8.35 ± 1.53	9.68 ± 0.06	9.67 ± 0.05	7.55 ± 2.08	9.60 ± 0.04	9.59 ± 0.04
Al	11.42 ± 1.47	11.00 ± 0.01	11.01 ± 0.01	10.67 ± 2.02	10.75 ± 0.10	10.76 ± 0.10
Zr	0.26 ± 1.70	0.30 ± 0.19	0.30 ± 0.23	0.24 ± 0.66	0.13 ± 0.01	0.13 ± 0.01
Y	5.99 ± 3.56	0.02 ± 0.02	0.08 ± 0.04	9.66 ± 6.73	0.03 ± 0.01	0.07 ± 0.02
O	8.45 ± 4.47	0.24 ± 0.02	0.33 ± 0.01	14.75 ± 9.46	0.17 ± 0.07	0.24 ± 0.15
C	0.19 ± 1.31	0.29 ± 0.03	0.29 ± 0.04	0.19 ± 0.47	0.10 ± 0.01	0.11 ± 0.01
N	0.01 ± 0.04	0.01 ± 0.09	0.01 ± 0.10	0.04 ± 0.08	0.02 ± 0.003	0.02 ± 0.003

due to uncorrected trajectory aberrations, but Y and O are clearly enriched in the precipitates in comparison to the surrounding matrix. Although the average Zr content is slightly enriched in these uncorrected compositions, this is primarily an artifact associated with co-precipitation of finer (Y,Al,O)-rich precipitates at the surface of larger (Zr,C)-rich precipitates, as it is clearly seen in the atom maps that the Zr is not locally enriched in this smaller precipitate population. It is important to note that the *matrix* composition reported in Table 2 refers to the volume not occupied by the fine-scale precipitates, so the increased Zr content in the matrix composition stems from the larger Zr-rich precipitates and is not due to Zr distributed homogeneously within the volume. The most difficult element to interpret is the Al content in the uncorrected precipitate compositions. Unlike ODS FeCr alloys—in which the only constituent elements in the precipitates are usually Y, Ti, and O, while the matrix comprises primarily Fe and Cr—in these ODS FeCrAl alloys, Al is both in the matrix and is a primary constituent in the smallest nanoprecipitates. Due to the significant trajectory aberrations included in these uncorrected cluster compositions, the local enrichment in Al illustrated in Fig. 4 is not captured in Table 2. This difficulty in assessing the Al content in the smallest nanoprecipitates is discussed later in Section 4.2.

If the Zr is not associated with the smallest nanoprecipitate population, then the primary question still exists as to what role this highly reactive element is performing within the microstructure. This question has been addressed in part through the identification of Zr- and C-rich precipitates in the previous control volumes, but a combination of both S/TEM + EDS and APT provided even more insight into this phenomenon. Fig. 5 shows the HAADF S/TEM image of 4H10C, in addition to multiple elemental EDS maps for various elements within the microstructure. It is immediately apparent that Al and Zr are both associated with impurity elements within the microstructure. Using multivariate statistical analysis (MVSA), the spatial and elemental overlaps were discretized and separated into two different populations of precipitates overlaid on the matrix component of the EDS spectrum (Fig. 5f). The corresponding map in Fig. 5g highlights an (Al,N)-rich precipitate population, in addition to a (Zr,C,N)-rich precipitate distribution. Thus, it appears that instead of competing with Al for Y and O in solution for the formation of the smallest nanoprecipitates, Zr competes for the C and N in solution for the formation of carbonitrides.

In addition to the S/TEM + EDS results, two additional APT control volumes were able to capture secondary populations of precipitates within the CrAZY annealed powder. As presented in Fig. 6a, a variety of different precipitates with varied compositions can be identified in one of the ZY10C60 control volumes. In addition to the smallest (Y,Al,O)-rich precipitates shown in red, two Zr-rich precipitates were identified and analyzed using 1D concentration profiles through each. From the profile in Fig. 6b, the equal concentrations of Zr and C at the precipitate core suggest that this is a ZrC precipitate of the MX type. However, the Zr-rich precipitate at the bottom of the control volume shows a different composition. The concentration profile in Fig. 6c indicates that this Zr-rich precipitate has a core/shell structure in which the core is primarily Zr(C,N) while the shell is ZrC. The last type of precipitate highlighted in this control volume is Cr- and Fe-rich. Comparing the sum of the Fe and Cr contents at the core of the precipitate with the C content provides a ratio consistent with a $M_{23}C_6$ precipitate. This is an important observation, because it provides the framework for explaining the role of C and N in the precipitation of the different

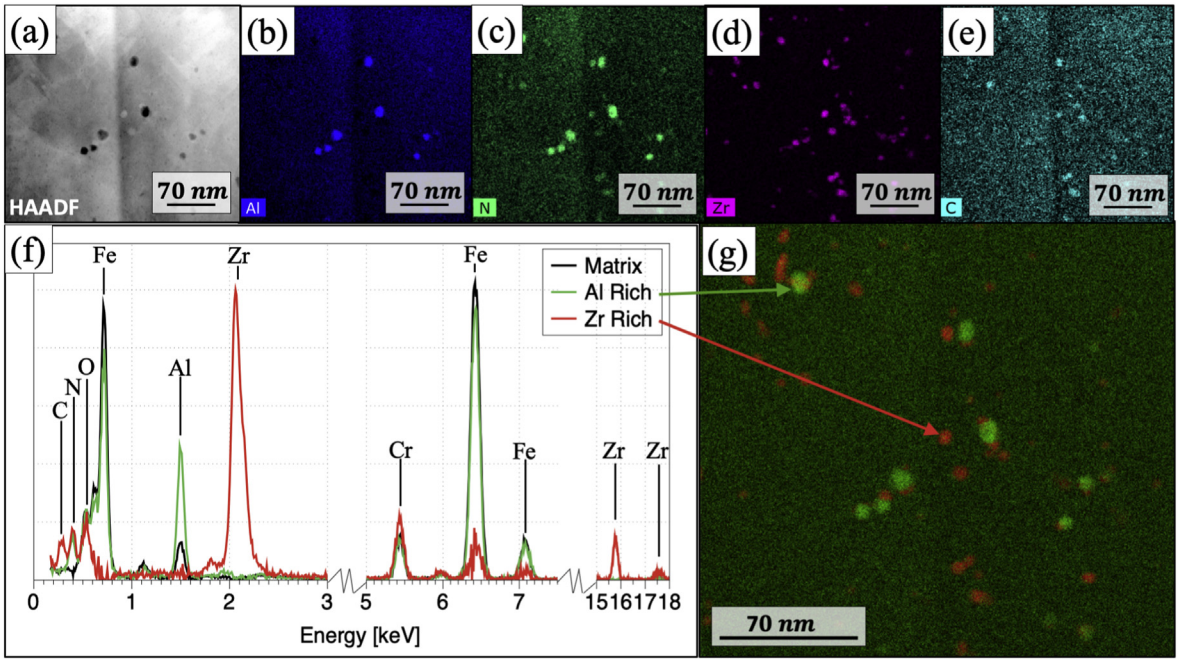

Fig. 5. S/TEM + EDS results for extruded alloy 4H10C. In addition to the (a) HAADF image investigated, elemental maps of (b) Al, (c) N, (d) Zr, and (e) C are highlighted. MVSA results have highlighted two different precipitate dispersions enriched in Al (green) and Zr (red), which are illustrated using the (f) EDS spectra and (g) corresponding EDS maps. (For interpretation of the references to color in this figure legend, the reader is referred to the Web version of this article.)

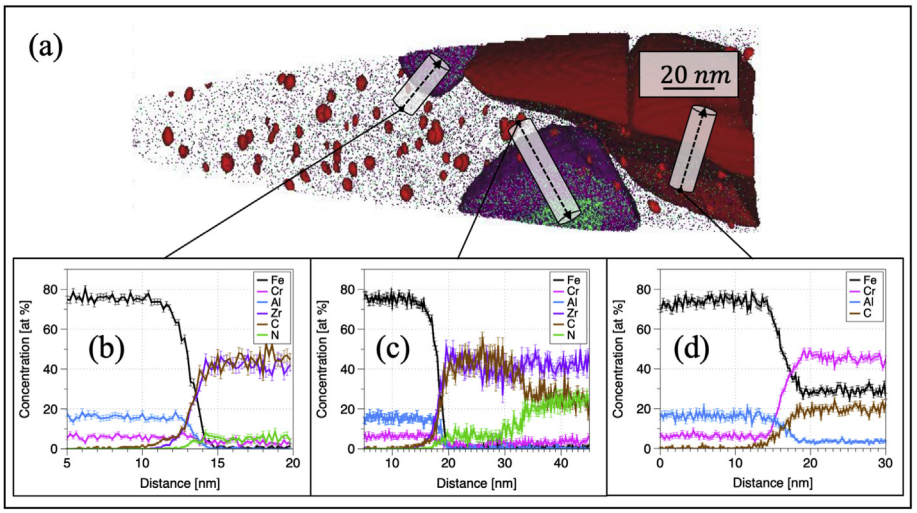

Fig. 6. An (a) APT control volume of ZY10C60 annealed powder with multiple types of precipitates atop black Fe matrix atoms. Red 1.5 at.% (Y,Al,O) isoconcentration surfaces highlight the smallest precipitate population, while brown 20 at.% Cr isoconcentration surfaces and purple 10 at.% Zr isoconcentration surfaces show larger precipitates in the volume. 1D concentration profiles through larger precipitates provide evidence for (b) ZrC, (c) Zr(C,N), and (d) $(Fe,Cr)_{23}C_6$. (For interpretation of the references to color in this figure legend, the reader is referred to the Web version of this article.)

distributions of dispersed phases within the CrAZY alloy. The core/shell structure of the Zr(C,N)-rich precipitate suggests that during the nucleation and growth stage of this phase, the local N content was depleted so that Zr, Cr, and C only remained for competition between these elements. As more and more Zr reacted with C within the microstructure, and was consumed by reaction with C, any remaining excess C apparently reacted with Fe and Cr to form the $M_{23}C_6$ carbide phase.

The final APT control volume that captured Zr sequestration of impurity elements indicates another interesting find, as depicted in Fig. 7a. This APT specimen, in addition to the red (Y,Al,O)-rich phases comprising the finest distribution of dispersed precipitates, has two coarser precipitates enriched primarily in (Al,O) and (Zr,C). A more detailed investigation of segregation of Y and YO ionic species shown in Fig. 7b indicates a qualitative enrichment of Y along the periphery of the coarse, Al-rich precipitate. A 1D concentration profile overlaid with the previous image (Fig. 7c) verifies that the Al-rich precipitate is consistent with an Al_2O_3 particle (likely present in the microstructure prior to powder annealing), while the Zr-rich precipitate is confirmed as ZrC. Also highlighted is

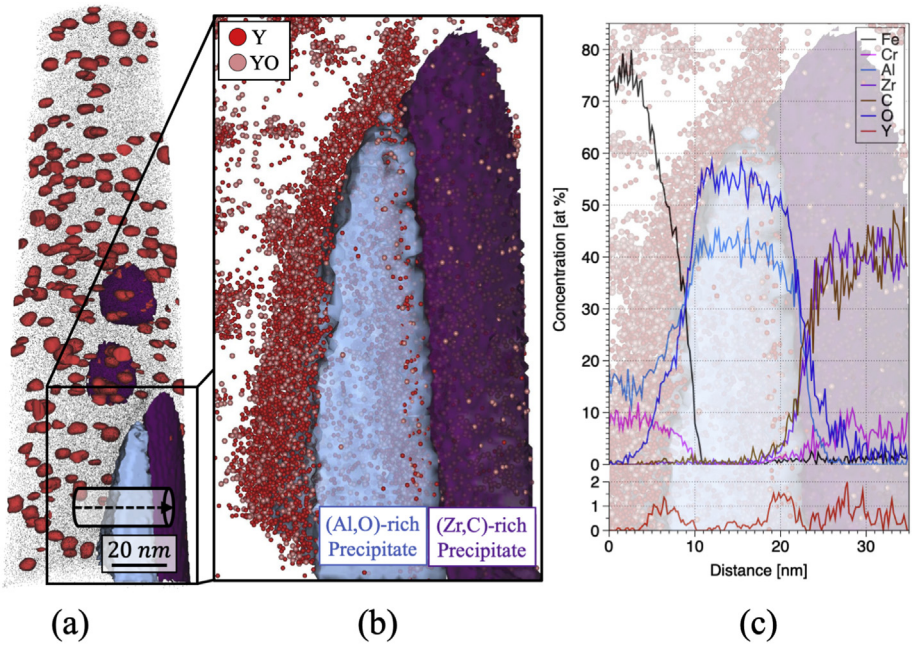

Fig. 7. An (a) APT control volume of ZY10C60 annealed powder with red 1.5 at.% (Y,Al,O) isoconcentration surfaces show fine-scale precipitation in addition to two larger precipitates. In (b) overlaid Y and YO atom maps atop 25 at.% Al and 10 at.% Zr isoconcentration surfaces identify co-precipitation in this volume. In (c), a 1D concentration profile shows these precipitates to be ZrC and Al_2O_3 with Y segregation to the surface of the alumina precipitate. (For interpretation of the references to color in this figure legend, the reader is referred to the Web version of this article.)

the preferential segregation of Y and YO ionic species to the surface of the Al_2O_3 particle, while the same segregation is not noted for the Zr-rich particle. This result indicates that, while the Zr preferentially reacted with C in the matrix and not Y and O, the high affinity of Al to react to form stable (Y,Al,O) complex oxides drove segregation of Y and O to the surface of the Al-rich precipitate.

These results strongly suggest that when interstitial elements such as C and N exist in the matrix, Zr will preferentially react with these elements instead of competing with Al for the formation of (Zr,Y,O)-rich precipitates previously reported by Dou and colleagues on similar ODS FeCrAlZr alloys [19]. The following section discusses testing of this hypothesis through the use of computational thermodynamics.

4. Discussion

4.1. Thermodynamic assessment of Zr precipitation

When assessing the affinity to react preferentially with Y and O in solution to form finer nanoscale oxides, previous researchers have used Ellingham diagrams to justify why (Zr,Y,O)-rich precipitates form preferentially in ODS FeCrAl alloys in comparison to (Y,Al,O)-rich precipitates. Although this is a completely valid design methodology for these alloys, the uni-dimensional nature of these analyses does not account for the potential impact of other reactive impurity elements such as C and N. A more robust method requires using the CALPHAD approach [47] to model precipitate stability in these alloys. Originally coined as the *Calculation of Phase Diagrams* (CALPHAD), this methodology has been extended to the computer coupling of phase diagrams and thermochemistry, whereby all available thermodynamic data and experimental phase diagrams for constituent elements are combined in a semi-empirical model to describe multi-component systems [48,49]. In this work, the CALPHAD approach was implemented using the ThermoCalc software [50] to predict equilibrium phases that should exist in the current CrAZY alloy system based on the measured composition of the extruded 4H10C alloy listed in Table 1.

Using the TCFE9 database within the ThermoCalc software, which includes all of the elements comprising the CrAZY alloy, the expected phase equilibria were calculated as a function of thermomechanical processing temperature based on the minimization of the Gibbs energy of the system for given conditions. Two scenarios were investigated for the current alloy system: (1) C and N are present, and (2) no C and N exist in the material. This way, the previously stated hypothesis that Zr preferentially will react with C and N instead of O in the matrix can be directly modeled.

Consistent with the previous experimental observations, the computational thermodynamics results indicate a strong effect of (C,N) solute impurities on equilibrium phases within the microstructure. When C and N are present in the matrix (Fig. 8a), the primary phases that are expected to form are Zr(C,N), AlN, Cr carbides, and complex (Y,Al,O)-rich oxides (orthorhombic yttrium aluminum perovskite YAP, and cubic yttrium aluminum garnet YAG). The experimental results would suggest that at 1000 °C, the smallest amount of precipitates is one of these two complex (Y,Al,O)-rich oxides, while the larger precipitate populations seen through APT and S/TEM are validated as Zr(C,N) and AlN. The calculation suggests that $(Cr,Fe)_7C_3$ is stable at 1000 °C, but in experiment, $(Cr,Fe)_{23}C_6$ was observed. This discrepancy suggests that either the thermodynamic modeling on the relative stability of these two carbides needs to be revised, or the $(Cr,Fe)_{23}C_6$ observed in the microstructure was transformed from $(Cr,Fe)_7C_3$ during the cooling process. In comparison, when C and N are removed completely from the material (Fig. 8b), the high affinity of both Zr and Al for O in solution results in a competition for the formation of $Zr_3Y_4O_{12}$ and YAP ($YAlO_3$) at the annealing/extrusion temperature of 1000 °C.

These results provide significant insights into the discrepancies

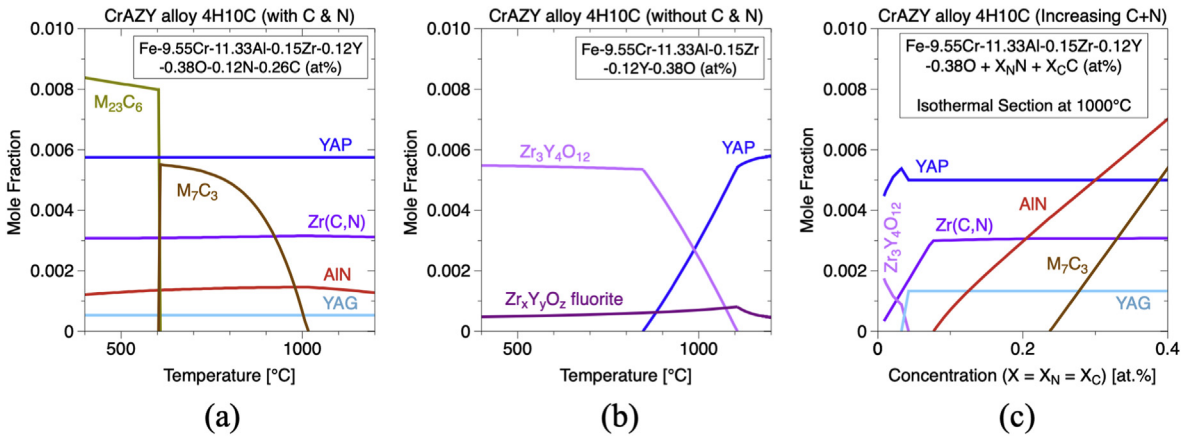

Fig. 8. Thermodynamic calculation results for expected CrAZY alloy phases in the 4H10C alloy (a) with and (b) without C and N impurity elements. Also shown in (c) is the effect of increasing C and N concentration on the equilibrium phases at 1000 °C.

that different researchers have found for the identities of the nanoprecipitates in ODS FeCrAlZr alloys [19,21]. In the alloy previously developed by Dou and colleagues [19], this competition is even stronger with respect to Zr for O since the Zr content of their alloy is doubled (0.37 at.%) in comparison to the alloy developed in this work (0.15 at.%). When this increase in Zr content is taken into consideration, the only complex oxide that would be expected to nucleate would be the $Zr_3Y_4O_{12}$ phase, which is consistent with the high resolution TEM results presented in the Dou study. This also suggests that the impurity C and N contents in the Dou alloy are lower than those introduced during the mechanical alloying stage in this work. To support this assertion, Fig. 8c illustrates the effect of increasing impurity C and N contents on the expected phases in our CrAZY alloy. With less than 0.1 at.% C and N added into solution, the low Zr content added to the present alloy is quickly sequestered, and the fraction of Al-rich oxides quickly increases in comparison to Zr-rich oxides.

With respect to alloy optimization and irradiation resistance, it has not yet been established which complex oxide is most beneficial in nuclear reactor applications. Recent comparisons of coarsening kinetics of (Y,Zr,O)- and (Y,Al,O)-rich precipitates at high temperature have suggested that although both complex oxides coarsen at faster rates than the (Y,Ti,O)-rich nanoprecipitates in ODS FeCr alloys, the coarsening kinetics of (Y,Al,O)-rich precipitates are somewhat slower [14]. However, future irradiation work must be performed on both alloys to determine which precipitate population provides improved resistance to ballistic dissolution. Furthermore, it remains unclear as to whether the secondary precipitate population of Zr(C,N) aids in the creep strength of these ODS FeCrAl alloys or if these precipitates deteriorate fracture properties by serving as pathways for crack propagation. These insights provide a framework for alloy design and comparison in future studies.

4.2. Insights on (Y,Al,O)-rich precipitate identities

Up to this point, the primary focus of this work has focused on the effect of Zr on precipitation in the CrAZY alloys, but the identities of the smallest nanoscale precipitates within these ODS FeCrAl alloys are equally important. Fig. 4 illustrates that the smallest nanoprecipitates were enriched in Y, Al, and O, as supported by computational thermodynamics results. However, multiple types of (Y,Al,O)-rich precipitates have been said to exist in a variety of fabricated ODS FeCrAl alloys, including yttrium aluminum tetragonal (YAT, $Y_3Al_5O_{12}$) [51,52], yttrium aluminum garnet (YAG, $Y_3Al_5O_{12}$) [21,53], yttrium aluminum perovskite (YAP, $YAlO_3$) [52–56], yttrium aluminum hexagonal (YAH, $YAlO_3$) [54], and yttrium aluminum monoclinic (YAM, $Y_4Al_2O_9$) [57,58]. With these discrepancies in the literature, it was thus undertaken to combine APT and high resolution S/TEM observations in an attempt to identify the specific precipitates that have nucleated in the current alloy system.

As mentioned above, all previous APT investigations of ODS Fe-based alloys have been limited to the FeCr system, in which the smallest precipitates are enriched in only Y, Ti, and O, and the surrounding matrix does not contain duplicate elements that can interfere with precipitate compositions after correcting for APT artifacts. Even in the case of ODS FeCr alloys, differences in APT compositions in comparison to expected stochiometric phases such as $Y_2Ti_2O_7$ and Y_2TiO_5 have sparked rigorous debate in the literature [42,59–68]. The current system increases the complexity of correcting these nanoprecipitate compositions drastically because the extent to which Al is partitioned between the precipitate and the matrix is unknown. If the matrix is subtracted out in proportion to erroneously high Fe and Cr contents, one may be subtracting out significant Al from the nanoprecipitates and fundamentally shifting the predicted nanoprecipitate compositions.

An attempt at cluster composition correction requires (1) the establishment of a methodology for systematically correcting for trajectory aberration artifacts and (2) an establishment of what to subtract from the precipitates. For ODS FeCr alloys, the “correction composition” was originally established as the measured matrix composition of the specimen [32]. Some authors have used TEM methods such as EELS and APT methods to identify what appears to be a Cr-rich shell surrounding the smallest (Y,Ti,O)-rich nanoprecipitates [32,69–71], resulting in a subtracted correction composition equal to the composition of the Cr-rich shell (80% Fe and 20% Cr in at.%). In this case, the methodology used for aberration correction is the recently developed CCC model [33], so the primary question is whether a similar Fe- and Cr-rich shell surrounds the (Y,Al,O)-rich precipitates in the current alloy system.

Consider two limiting cases shown in Fig. 9 that could exist after the assumed supersaturated solid solution of elements is heated and the nanoscale (Y,Al,O) precipitates nucleate and grow to stable sizes. In the first case, the nanoprecipitate nucleates such that only the matrix enriched in Fe, Cr, and Al surrounds the precipitate. In this case, when applying the CCC model, the correction matrix subtracted from the nanoprecipitate

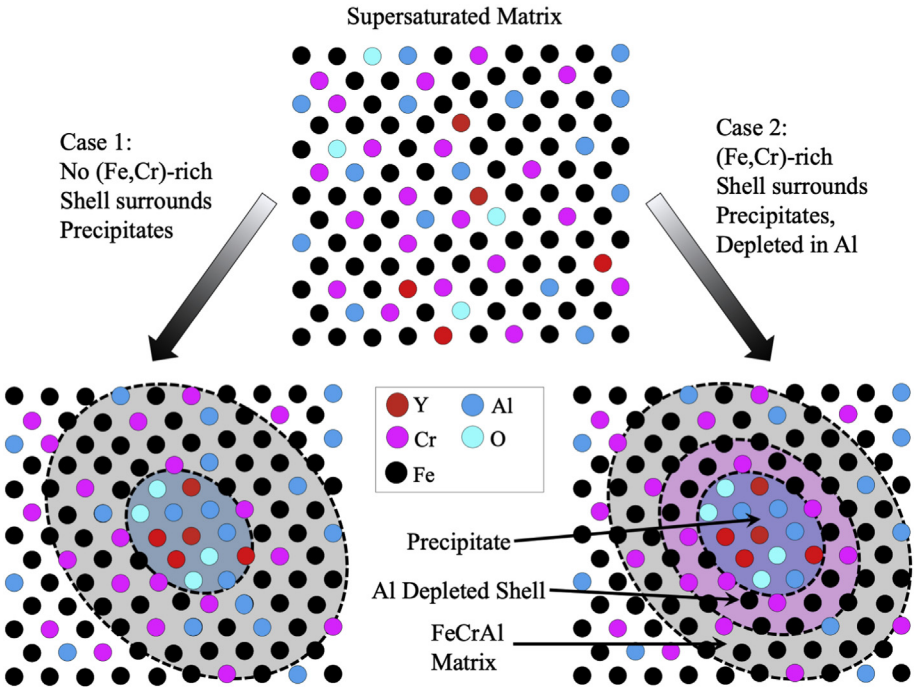

Fig. 9. Visualization of the two limiting cases for precipitate compositional correction.

composition will be equal to the matrix composition reported in Table 2. In the second case, the consumption of Al locally around the precipitate results in an Al-depleted region enriched in Fe and Cr only, which prevents significant Al from being subtracted from the nanoprecipitate compositions.

To determine which of these cases to use in the implementation of the CCC model, a combination of EELS and APT was used to assess potential Cr-enrichment surrounding precipitates in the CrAZY extruded alloy. In Fig. 10a, EELS was used on a representative precipitate 2 nm in diameter that appears in the HAADF image as a darker feature. The Fe and Cr maps across this precipitate show no significant variations, which suggests that although the thickness of the specimen was thin enough to resolve this nanoscale precipitate, significant through-thickness Fe and Cr contents make the EELS results insufficient to indicate the existence of a Cr-rich shell. As an alternative approach, an identical methodology to that implemented by London et al. [69] for a comparable model ODS FeCr alloy was implemented in Python. In this approach, for each individual precipitate, a control volume equal to the width of each precipitate was created around each precipitate with a length equal to 4 $\times$ the evaporation "z" direction through the precipitate. Then, 1D concentration profiles were recorded for each precipitate and normalized with respect to the total distance across each precipitate. In London's work, a clear enrichment of Cr was seen at the precipitate/matrix interface and was measured as high as 20 at.% for precipitates larger than 4 nm in diameter. The results of the APT analysis in the current study are presented in Fig. 10b, with results separated as a function of precipitate size. In contrast to the results on ODS FeCr alloys, the variation of Cr content across precipitates of all sizes did not exceed 1% in comparison to the surrounding matrix composition. These EELS and APT results do not support the existence of a Cr-rich shell surrounding the precipitates, so the compositional correction composition was assumed to be equal to that measured initially in the matrix surrounding the precipitates.

The implications of these results are depicted in Fig. 11. In Fig. 11a, the average modeled nanoprecipitate composition for the 342 nanoprecipitates in an APT control volume of CrAZY alloy 4H10C is shown as a function of the extent of compositional correction. After applying the CCC model, if there were a Cr-rich shell deplete of Al, then the average nanoprecipitate composition would have a Y/Al ratio similar to that expected for the YAG ($Y_3Al_5O_{12}$) complex oxide phase, although significantly underestimated in oxygen content. As the correction composition is changed from that of a Cr-rich shell to that only subtracting the as-measured matrix composition from the precipitates as a function of precipitate shape and atomic density variation, the average composition tends toward a phase consistent with YAM ($Y_4Al_2O_9$), and the O content is much less underestimated in comparison to the expected stochiometric phase. In Fig. 11b and Fig. 11c, each individual precipitate composition is plotted on the same ternary diagram for the limiting cases of a Cr-rich shell and for no shell, respectively. The diameter of each circle on the plot is scaled as a function of precipitate diameter. In addition, using the probability frequency of multiple points lying on the same point of the ternary diagram represented by the color bar under each figure, the compositions with the highest probability of occurrence are highlighted on each ternary diagram.

Even after applying the CCC model for correcting these precipitate compositions, significant spread still exists in the compositions of many of the identified precipitates. This may suggest that (1) a spread still exists in the types of (Y,Al,O)-rich precipitates that have nucleated during annealing or (2) even the most robust correction algorithms developed for ODS FeCr alloys such as the CCC model are imperfect for cases such as the current CrAZY alloy system where there is partitioning of certain elements between precipitates and the matrix.

One aspect of the CCC model that may be able to provide better clarity for nanoprecipitate compositions would be the inclusion of a term accounting for atoms of each element that are non-quantified during the field evaporation process. Unfortunately, without bulk

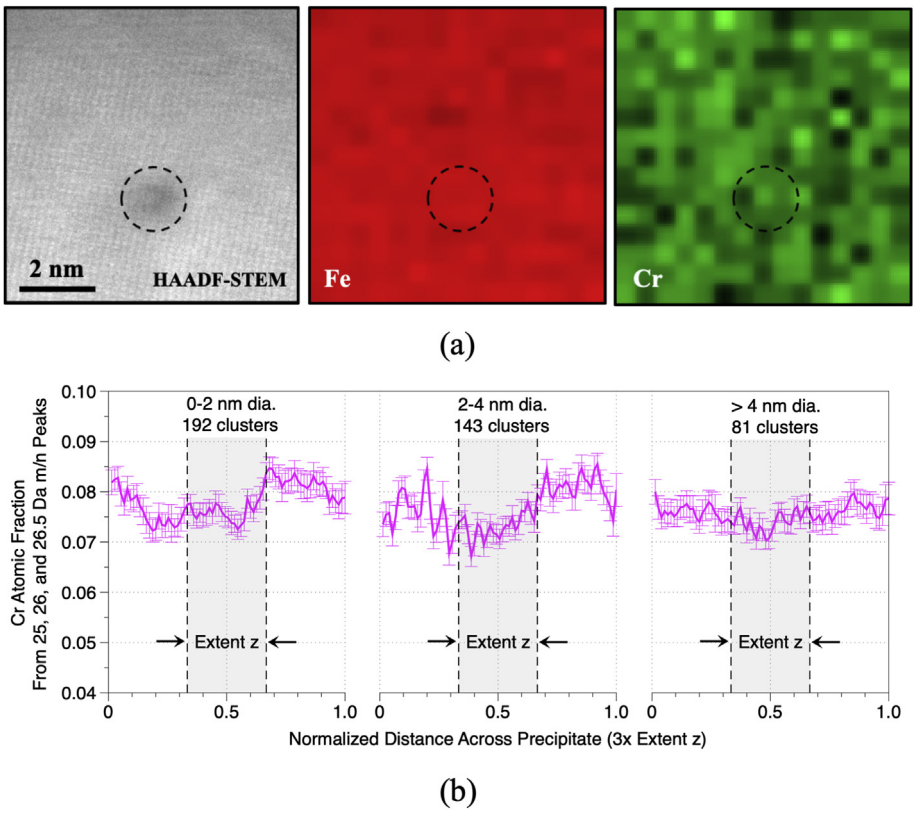

Fig. 10. (a) EELS results for a ~2 nm diameter precipitate in extruded alloy 4H10C showing insufficient evidence for a Cr-rich shell surrounding the identified precipitate, and (b) average normalized 1D concentration profiles taken from APT data through precipitates in CrAZY specimen ZY10C60 showing no detectable Cr-rich shell surrounding (Y,Al,O)-rich precipitates of different sizes. Error bars indicate 95% confidence intervals for the measured Cr concentration.

APT measurements on ternary (Y,Al,O) oxide phases, the unknown partitioning of Al between the matrix and the precipitates doesn't allow for the direct calculation of this term in the current analysis. Consequently, in an attempt to qualify the results of the CCC model applied to the APT data on the precipitates in 4H10C, high resolution S/TEM was conducted on the same sample. Multiple precipitates were successfully imaged, and FFTs of the S/TEM images were indexed to determine the likely phases from direct structural observations. Two of these precipitates are highlighted in Fig. 12. The measured d-spacings and angles are compared with tabulated values for compared stochiometric phases and are also reported in Table 3. One of the major challenges in the indexing of these FFT patterns is that many of the reflections between the different phases are similar with respect to angles, but luckily, both the d-spacings and measured angles could be compared simultaneously. The precipitate in Fig. 12a matches well to reflections for the YAM phase, while the precipitate in Fig. 12b matches to a structure consistent with the YAG phase. Errors for the d-spacings and angles for each precipitate were within 1–2% error, giving high confidence that both of these phases exist simultaneously in the CrAZY alloy. Unfortunately, these S/TEM results do not aid in the validation of either assumption used in the APT data correction algorithm. Instead, this result supports the spread in APT data, suggesting that a variety of different phases exist in the as-fabricated alloy [21,51–58].

The identified phases as measured using APT and S/TEM, YAM and YAG, differ from the phases calculated using computational thermodynamics. From the ThermoCalc results, it was predicted that the YAP phase would be more prevalent in the microstructure, with a small fraction of YAG also possible. In fact, the computational thermodynamics results suggest that no thermodynamic driving force is available in the formation of the YAM phase with respect to the current alloy composition if YAG and YAP are allowed to form. To put this into perspective, it is important to consider previous high-resolution TEM results from the literature, as well as local atomic concentrations within the material during annealing. Multiple researchers have asserted that the YAM phase exists for nanoscale precipitates in ODS FeCrAl alloys either in annealed powder or extruded alloys [57,72]. The argument for the preferential nucleation of this complex oxide has been previously framed with respect to a fundamental study comparing complex oxides that formed in a diffusion bond between yttria and alumina at high temperature [73]. In this study, it was found that the formation of the complex oxides was limited by the rate at which Al diffused into yttria. Consequently, the first complex oxide formed (at the lowest temperature of 900–1100 °C) was that of the largest ratio of Y to Al, or YAM. Then at higher temperatures YAP and YAG would form, respectively, as the ratio of Y/Al decreased as more Al diffused into yttria. This is a somewhat flawed argument in the sense that in these ODS FeCrAl alloys, assuming a solid solution after mechanically alloying, the ratio of Y to Al is quite small since only a small amount of yttria was initially added to a matrix heavily enriched in Al. This is supported by a study in which different proportions of alumina and yttria were ball-milled and then annealed at high temperature. Depending on the ratio of alumina to yttria, the preferential phases formed were consistent with the ratio of Y to Al expected for each complex oxide phase [74]. From this perspective, YAG would be expected to

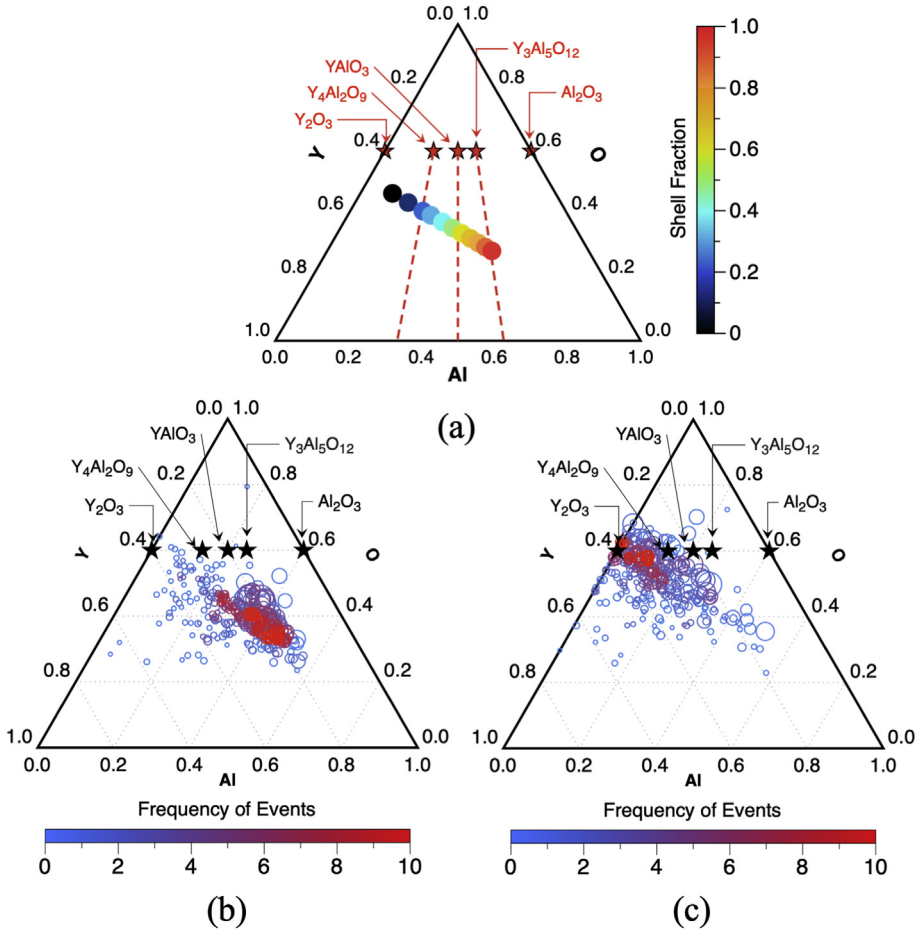

Fig. 11. Ternary diagrams showing (a) the variation of average (Y,Al,O)-rich composition as a function of the surrounding environment used for compositional correction, as well as individual precipitate compositions for alloy 4H10C corrected with (b) a (80% Fe, 20%Cr in at.%) shell surrounding each precipitate and (c) no shell influencing the matrix composition surrounding individual precipitates. Color bars in b–c indicate the probability of finding multiple precipitates with a certain composition in the respective ternary diagram. (For interpretation of the references to color in this figure legend, the reader is referred to the Web version of this article.)

preferentially form from a supersaturated solid solution instead of YAM for the current ODS FeCrAl alloy system.

To resolve these differences, a new mechanism is proposed that considers the extent to which mechanical alloying has successfully driven Y into solid solution in the ODS FeCrAl matrix. It has been previously shown that after the mechanical alloying step in ODS FeCr alloys, Y is not fully in solid solution, and instead there are YO-rich clusters (<1 nm in size) at a much higher number density in comparison to the annealed powder after further growth and coarsening of the smallest oxide particles [66]. From this perspective, not only is there the potential for a partial solid solution of Y in the matrix, but there are also many clusters that are highly enriched in Y and O that would only require Al diffusion to the clusters to form a complex oxide. If a cluster is already enriched mostly in Y, then the ratio of Y/Al during the initial growth of the cluster would be higher, allowing for YAM to form. In contrast, for regions with Y in solid solution, the YAG phase would preferentially form. This would result in a variety of complex (Y,Al,O) oxide phases forming during the initial stages of nucleation and growth, providing evidence that the many oxide phases noted in the literature may all exist simultaneously, depending on the local concentrations of elements in the as-milled ODS FeCrAl powder during annealing and subsequent consolidation.

5. Conclusions

In this study, a detailed investigation of the types of precipitates in annealed powders and consolidated ODS FeCrAl CrAZY alloys was performed. Using detailed APT characterization, a high number density of (Y,Al,O)-rich nanoprecipitates with number densities exceeding 10^{23} m^{-3} and diameters in the 2–4 nm range were identified. Through computational thermodynamic modeling, it was found that the alloy composition—notably impurity C and N contents—are highly influential in the types of precipitates that form after alloy consolidation. When C and N are present in the matrix, highly reactive alloying elements such as Zr preferentially form MX-type carbonitride phases and compete with Al and Cr in the matrix for these interstitial elements. When impurity elements C and N are low, Zr competes with Al in the matrix to form the smallest complex oxides that give these ODS FeCrAl alloys their beneficial properties. Using the state-of-the-art compositional correction models available in literature for ODS FeCr alloys, a parametric investigation of (Y,Al,O)-rich precipitate compositions was performed, stressing the need for specific methodologies for considering element partitioning between the precipitate and the surrounding matrix. A combination of high-resolution S/TEM and APT indicates that many types of precipitate phases can exist in ODS FeCrAl alloys simultaneously with precipitates enriched in Y, Al, and O. With these results in perspective,

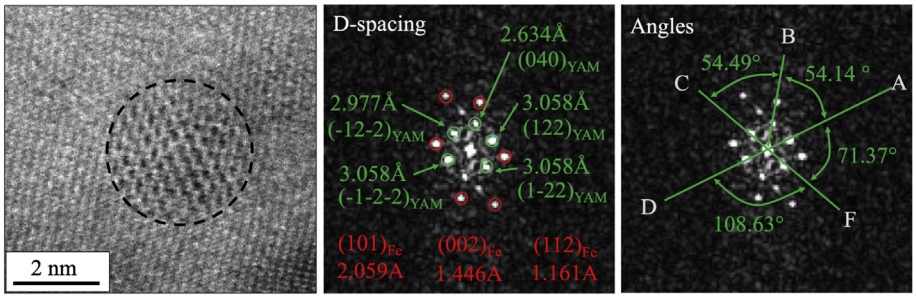

(a) Identified precipitate consistent with YAM

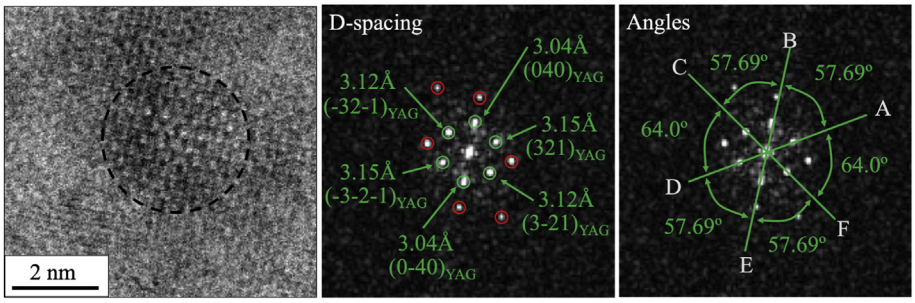

(a) Identified precipitate consistent with YAG

Fig. 12. High-resolution S/TEM images of select nanoscale precipitates in the CrAZY extruded alloy 4H10C, showing examples of precipitates matching the structure of (a) YAM and (b) YAG.

Table 3
Comparison of measured inter-planar distances (d) and angles (α) for precipitates shown in Fig. 12 with respect to tabulated ICDD values for YAG (PDF# 00-033-0040) and YAM (PDF# 00-022-0987).

Precipitate 1 – Fig. 12a								
d-spacing Comparison					Angles Comparison			
Location	Measured (Å)	Reflection	Tabulated (Å)	Error (%)	Angle	Measured (°)	Tabulated (°)	Error (%)
d_A	3.058	$(122)_{YAM}$	3.01	1.59	α_{AB}	54.15	54.85	1.28
d_B	2.634	$(040)_{YAM}$	2.615	0.73	α_{BC}	54.49	54.85	0.66
d_C	2.977	$(-12-2)_{YAM}$	3.01	1.10	α_{CD}	71.37	70.28	1.55
d_D	3.058	$(-1-2-2)_{YAM}$	3.01	1.59	α_{DF}	108.63	109.7	0.98
d_E	2.634	$(0-40)_{YAM}$	2.615	0.73				
d_F	2.977	$(1-22)_{YAM}$	3.01	1.10				
Precipitate 2 – Fig. 12b								
d-spacing Comparison					Angles Comparison			
Location	Measured (Å)	Reflection	Tabulated (Å)	Error (%)	Angle	Measured (°)	Tabulated (°)	Error (%)
d_A	3.15	$(321)_{YAG}$	3.210	1.87	α_{AB}	57.69	57.68	0.02
d_B	3.04	$(040)_{YAG}$	3.002	1.27	α_{BC}	57.69	57.68	0.02
d_C	3.12	$(-32-1)_{YAG}$	3.210	2.80	α_{CD}	64	64.6	0.93
d_D	3.15	$(-3-2-1)_{YAG}$	3.210	1.87	α_{DE}	57.69	57.68	0.02
d_E	3.04	$(0-40)_{YAG}$	3.002	1.27	α_{EF}	57.69	57.68	0.02
d_F	3.12	$(3-21)_{YAG}$	3.210	2.80				

new ODS FeCrAl alloys can be developed, with an integral understanding of how compositional variations can change alloy properties and potentially the viability of these alloys in extreme environments associated with advanced nuclear reactor applications.

Data availability statement

The raw/processed data required to reproduce these findings will be made available upon request.

Declaration of competing interest

The authors declare that they have no known competing financial interests or personal relationships that could have appeared to influence the work reported in this paper.

CRediT authorship contribution statement

Caleb P. Massey: Conceptualization, Investigation, Formal analysis, Data curation, Writing - original draft. **Philip D. Edmondson:** Methodology, Software, Resources, Investigation, Writing - review & editing. **Kinga A. Unocic:** Formal analysis, Writing - review & editing. **Ying Yang:** Formal analysis, Data curation. **Sebastien N. Dryepondt:** Methodology, Project administration, Writing - review & editing. **Anoop Kini:** Investigation. **Baptiste Gault:** Supervision, Visualization, Resources. **Kurt A. Terrani:** Project administration. **Steven J. Zinkle:**

Supervision, Resources, Writing - review & editing.

Acknowledgments

The work presented in this paper was supported primarily by the Advanced Fuels Campaign of the Nuclear Technology R&D program in the Office of Nuclear Energy, US Department of Energy. This work was also funded in part by the Office of Fusion Energy Sciences. This manuscript has been authored by Oak Ridge National Laboratory, managed by UT-Battelle, LLC, under Contract No. DE-AC05-00OR22725 with the U.S. Department of Energy. A portion of this work was conducted using the FEI Talos F200X S/TEM tool provided by US DOE, Office of Nuclear Energy, Fuel Cycle R&D Program and the Nuclear Science User Facilities. Microscopy performed as part of a user project at the Center for Nanophase Materials Sciences (CNMS), which is sponsored by the Scientific User Facilities Division, Office of Basic Energy Sciences, U.S. Department of Energy. D. W. Coffey assisted with the experimental work. The authors would like to thank Tom Geer for metallographic sample preparation and to Gregory Cox for extruding the powder material. Finally, we would like to thank and acknowledge Karren More for her insight and critical review of our manuscript during its preparation.

Appendix A. Supplementary data

Supplementary data to this article can be found online at https://doi.org/10.1016/j.jnucmat.2020.152105.

References

[1] G. Korb, M. Rühle, H.-P. Martinz, New Iron-Based ODS-Superalloys for High Demanding Applications, ASME 1991 International Gas Turbine and Aeroengine Congress and Exposition, American Society of Mechanical Engineers, 1991. V005T12A015-V005T12A015.
[2] S. Dryepondt, A. Rouaix-Vande Put, B.A. Pint, Effect of H2O and CO2 on the oxidation behavior and durability at high temperature of ODS-FeCrAl, Oxid. Metals 79 (5) (2013) 627–638.
[3] L. Marechal, B. Lesage, A. Huntz, R. Molins, Oxidation behavior of ODS Fe–Cr–Al alloys: aluminum depletion and lifetime, Oxid. Metals 60 (1–2) (2003) 1–28.
[4] S.J. Zinkle, L.L. Snead, Designing radiation resistance in materials for fusion energy, Annu. Rev. Mater. Res. 44 (1) (2014) 241–267.
[5] B.A. Pint, K.A. Terrani, M.P. Brady, T. Cheng, J.R. Keiser, High temperature oxidation of fuel cladding candidate materials in steam–hydrogen environments, J. Nucl. Mater. 440 (1–3) (2013) 420–427.
[6] K.A. Terrani, S.J. Zinkle, L.L. Snead, Advanced oxidation-resistant iron-based alloys for LWR fuel cladding, J. Nucl. Mater. 448 (1–3) (2014) 420–435.
[7] S. Dryepondt, K.A. Unocic, D.T. Hoelzer, C.P. Massey, B.A. Pint, Development of low-Cr ODS FeCrAl alloys for accident-tolerant fuel cladding, J. Nucl. Mater. 501 (2018) 59–71.
[8] Y. Yano, T. Tanno, H. Oka, S. Ohtsuka, T. Inoue, S. Kato, T. Furukawa, T. Uwaba, T. Kaito, S. Ukai, N. Oono, A. Kimura, S. Hayashi, T. Torimaru, Ultra-high temperature tensile properties of ODS steel claddings under severe accident conditions, J. Nucl. Mater. 487 (2017) 229–237.
[9] C.P. Massey, P.D. Edmondson, K.G. Field, D.T. Hoelzer, S.N. Dryepondt, K.A. Terrani, S.J. Zinkle, Post irradiation examination of nanoprecipitate stability and α′ precipitation in an oxide dispersion strengthened Fe-12Cr-5Al alloy, Scripta Mater. 162 (2019) 94–98.
[10] B.A. Pint, S. Dryepondt, K.A. Unocic, D.T. Hoelzer, Development of ODS FeCrAl for compatibility in fusion and fission energy applications, JOM 66 (12) (2014) 2458–2466.
[11] C.H. Zhang, J. Jang, H.D. Cho, Y.T. Yang, Void swelling in MA956 ODS steel irradiated with 122MeV Ne-ions at elevated temperatures, J. Nucl. Mater. 386–388 (2009) 457–461.
[12] M.B. Toloczko, D.S. Gelles, F.A. Garner, R.J. Kurtz, K. Abe, Irradiation creep and swelling from 400 to 600 °C of the oxide dispersion strengthened ferritic alloy MA957, J. Nucl. Mater. 329–333 (2004) 352–355.
[13] N. Oono, K. Nakamura, S. Ukai, T. Kaito, T. Torimaru, A. Kimura, S. Hayashi, Oxide particle coarsening at temperature over 1473 K in 9CrODS steel, Nucl. Mater. Energy 9 (2016) 342–345.
[14] N.H. Oono, S. Ukai, S. Hayashi, S. Ohtsuka, T. Kaito, A. Kimura, T. Torimaru, K. Sakamoto, Growth of oxide particles in FeCrAl- oxide dispersion strengthened steels at high temperature, J. Nucl. Mater. 493 (2017) 180–188.
[15] N. Cunningham, Y. Wu, D. Klingensmith, G.R. Odette, On the remarkable thermal stability of nanostructured ferritic alloys, Mater. Sci. Eng., A 613 (2014) 296–305.
[16] C.P. Massey, S.N. Dryepondt, P.D. Edmondson, M.G. Frith, K.C. Littrell, A. Kini, B. Gault, K.A. Terrani, S.J. Zinkle, Multiscale investigations of nanoprecipitate nucleation, growth, and coarsening in annealed low-Cr oxide dispersion strengthened FeCrAl powder, Acta Mater. 166 (2019) 1–17.
[17] C.P. Massey, S.L. Dryepondt, P.D. Edmondson, K.A. Terrani, S.J. Zinkle, Influence of mechanical alloying and extrusion conditions on the microstructure and tensile properties of low-Cr ODS FeCrAl alloys, J. Nucl. Mater. 512 (2018) 227–238.
[18] P. Dou, A. Kimura, T. Okuda, M. Inoue, S. Ukai, S. Ohnuki, T. Fujisawa, F. Abe, Effects of extrusion temperature on the nano-mesoscopic structure and mechanical properties of an Al-alloyed high-Cr ODS ferritic steel, J. Nucl. Mater. 417 (1–3) (2011) 166–170.
[19] P. Dou, A. Kimura, R. Kasada, T. Okuda, M. Inoue, S. Ukai, S. Ohnuki, T. Fujisawa, F. Abe, TEM and HRTEM study of oxide particles in an Al-alloyed high-Cr oxide dispersion strengthened steel with Zr addition, J. Nucl. Mater. 444 (1–3) (2014) 441–453.
[20] P. Dou, A. Kimura, R. Kasada, T. Okuda, M. Inoue, S. Ukai, S. Ohnuki, T. Fujisawa, F. Abe, S. Jiang, Z. Yang, TEM and HRTEM study of oxide particles in an Al-alloyed high-Cr oxide dispersion strengthened ferritic steel with Hf addition, J. Nucl. Mater. 485 (2017) 189–201.
[21] K.A. Unocic, B.A. Pint, D.T. Hoelzer, Advanced TEM characterization of oxide nanoparticles in ODS Fe–12Cr–5Al alloys, J. Mater. Sci. 51 (20) (2016) 9190–9206.
[22] M.K. Miller, K.F. Russell, Atom probe specimen preparation with a dual beam SEM/FIB miller, Ultramicroscopy 107 (9) (2007) 761–766.
[23] D. Vaumousse, A. Cerezo, P. Warren, A procedure for quantification of precipitate microstructures from three-dimensional atom probe data, Ultramicroscopy 95 (2003) 215–221.
[24] A. Cerezo, L. Davin, Aspects of the observation of clusters in the 3-dimensional atom probe, Surf. Interface Anal. 39 (2-3) (2007) 184–188.
[25] L.T. Stephenson, M.P. Moody, P.V. Liddicoat, S.P. Ringer, New techniques for the analysis of fine-scaled clustering phenomena within atom probe tomography (APT) data, Microsc. Microanal. 13 (6) (2007) 448–463.
[26] E.A. Marquis, J.M. Hyde, Applications of atom-probe tomography to the characterisation of solute behaviours, Mater. Sci. Eng. R Rep. 69 (4–5) (2010) 37–62.
[27] D.J. Larson, T. Prosa, R.M. Ulfig, B.P. Geiser, T.F. Kelly, Local Electrode Atom Probe Tomography, Springer Science, New York, US, 2013.
[28] B. Gault, M.P. Moody, J.M. Cairney, S.P. Ringer, Atom Probe Microscopy, Springer, 2012.
[29] P.D. Edmondson, S.A. Briggs, Y. Yamamoto, R.H. Howard, K. Sridharan, K.A. Terrani, K.G. Field, Irradiation-enhanced α′ precipitation in model FeCrAl alloys, Scripta Mater. 116 (2016) 112–116.
[30] D. Blavette, F. Vurpillot, P. Pareige, A. Menand, A model accounting for spatial overlaps in 3D atom-probe microscopy, Ultramicroscopy 89 (1–3) (2001) 145–153.
[31] C. Hatzoglou, B. Radiguet, P. Pareige, Experimental artefacts occurring during atom probe tomography analysis of oxide nanoparticles in metallic matrix: quantification and correction, J. Nucl. Mater. 492 (2017) 279–291.
[32] C.A. Williams, E.A. Marquis, A. Cerezo, G.D.W. Smith, Nanoscale characterisation of ODS–Eurofer 97 steel: an atom-probe tomography study, J. Nucl. Mater. 400 (1) (2010) 37–45.
[33] C. Hatzoglou, B. Radiguet, F. Vurpillot, P. Pareige, A chemical composition correction model for nanoclusters observed by APT - application to ODS steel nanoparticles, J. Nucl. Mater. 505 (2018) 240–248.
[34] C.M. Parish, N.K. Kumar, L.L. Snead, P.D. Edmondson, K.G. Field, C. Silva, A.M. Williams, K. Linton, K.J. Leonard, LAMDA, Irradiated-materials microscopy at Oak Ridge national laboratory, Microsc. Microanal. 21 (S3) (2015) 1003–1004.
[35] C.M. Parish, MT3FT-15OR0204122: Report on the Acquisition and Installation of FEI Talos F200X S/TEM, Oak Ridge National Laboratory (ORNL), Oak Ridge, TN (United States), 2015.
[36] H. Von Harrach, P. Dona, B. Freitag, H. Soltau, A. Niculae, M. Rohde, An integrated silicon drift detector system for FEI Schottky field emission transmission electron microscopes, Microsc. Microanal. 15 (S2) (2009) 208.
[37] P.G. Kotula, M.R. Keenan, J.R. Michael, Automated analysis of SEM X-ray spectral images: a powerful new microanalysis tool, Microsc. Microanal. 9 (1) (2003) 1–17.
[38] N. Sallez, Recrystallization, Abnormal Grain Growth and Ultrafine Microstructure of ODS Ferritic Steels, Materials, PhD Thesis, Université de Grenoble, 2014.
[39] A. Deschamps, F. De Geuser, J. Malaplate, D. Sornin, When do oxide precipitates form during consolidation of oxide dispersion strengthened steels? J. Nucl. Mater. 482 (2016) 83–87.
[40] D.T. Hoelzer, K.A. Unocic, M.A. Sokolov, T.S. Byun, Influence of processing on the microstructure and mechanical properties of 14YWT, J. Nucl. Mater. 471 (2016) 251–265.
[41] M.K. Miller, D.T. Hoelzer, Effect of neutron irradiation on nanoclusters in MA957 ferritic alloys, J. Nucl. Mater. 418 (1–3) (2011) 307–310.
[42] M.K. Miller, D.T. Hoelzer, E.A. Kenik, K.F. Russell, Nanometer scale precipitation in ferritic MA/ODS alloy MA957, J. Nucl. Mater. 329–333 (2004) 338–341.
[43] M. Bachhav, G. Robert Odette, E.A. Marquis, α′ precipitation in neutron-irradiated Fe–Cr alloys, Scripta Mater. 74 (2014) 48–51.

[44] S.A. Briggs, P.D. Edmondson, K.C. Littrell, Y. Yamamoto, R.H. Howard, C.R. Daily, K.A. Terrani, K. Sridharan, K.G. Field, A combined APT and SANS investigation of α′ phase precipitation in neutron-irradiated model FeCrAl alloys, Acta Mater. 129 (2017) 217–228.
[45] P.D. Edmondson, C.M. Parish, R.K. Nanstad, Using complimentary microscopy methods to examine Ni-Mn-Si-precipitates in highly-irradiated reactor pressure vessel steels, Acta Mater. 134 (2017) 31–39.
[46] M.K. Miller, Atom Probe Tomography: Analysis at the Atomic Level, Springer Science & Business Media2012.
[47] L. Kaufman, H. Bernstein, Computer Calculation of Phase Diagrams. With Special Reference to Refractory Metals, 1970.
[48] N. Saunders, CALPHAD (Calculation of Phase Diagrams): a Comprehensive Guide, 1998. Oxford, New York.
[49] A. Kroupa, Modelling of phase diagrams and thermodynamic properties using Calphad method: development of thermodynamic databases, Comput. Mater. Sci. 66 (2013) 3–13.
[50] J.-O. Andersson, T. Helander, L. Höglund, P. Shi, B.J.C. Sundman, Thermo-calc & DICTRA, Comput. Tools Mater. Sci. 26 (2) (2002) 273–312.
[51] B. Dubiel, W. Osuch, M. Wróbel, P. Ennis, A. Czyrska-Filemonowicz, Correlation of the microstructure and the tensile deformation of incology MA956, J. Mater. Process. Technol. 53 (1–2) (1995) 121–130.
[52] H. Cama, T. Hughes, Stability of dispersoids in commercially available mechanically alloyed oxide dispersion strengthened alloys after high temperature exposures, Mater. Adv. Power Eng., Part II (1994) 1497–1506.
[53] C. Chen, P. Wang, G. Tatlock, Phase transformations in yttrium–aluminium oxides in friction stir welded and recrystallised PM2000 alloys, Mater. A. T. High. Temp. 26 (3) (2009) 299–303.
[54] P. Dou, A. Kimura, T. Okuda, M. Inoue, S. Ukai, S. Ohnuki, T. Fujisawa, F. Abe, Polymorphic and coherency transition of Y–Al complex oxide particles with extrusion temperature in an Al-alloyed high-Cr oxide dispersion strengthened ferritic steel, Acta Mater. 59 (3) (2011) 992–1002.
[55] M. Klimiankou, R. Lindau, A. Möslang, J. Schröder, TEM study of PM 2000 steel, Powder Metall. 48 (3) (2013) 277–287.
[56] C.H. Zhang, A. Kimura, R. Kasada, J. Jang, H. Kishimoto, Y.T. Yang, Characterization of the oxide particles in Al-added high-Cr ODS ferritic steels, J. Nucl. Mater. 417 (1–3) (2011) 221–224.
[57] L.L. Hsiung, M.J. Fluss, A. Kimura, Structure of oxide nanoparticles in Fe–16Cr MA/ODS ferritic steel, Mater. Lett. 64 (16) (2010) 1782–1785.
[58] L.L. Hsiung, M.J. Fluss, S.J. Tumey, B.W. Choi, Y. Serruys, F. Willaime, A. Kimura, Formation mechanism and the role of nanoparticles in Fe-Cr ODS steels developed for radiation tolerance, Phys. Rev. B 82 (18) (2010) 184103.
[59] A.J. London, S. Santra, S. Amirthapandian, B.K. Panigrahi, R.M. Sarguna, S. Balaji, R. Vijay, C.S. Sundar, S. Lozano-Perez, C.R.M. Grovenor, Effect of Ti and Cr on dispersion, structure and composition of oxide nano-particles in model ODS alloys, Acta Mater. 97 (2015) 223–233.
[60] Y. Wu, E.M. Haney, N.J. Cunningham, G.R. Odette, Transmission electron microscopy characterization of the nanofeatures in nanostructured ferritic alloy MA957, Acta Mater. 60 (8) (2012) 3456–3468.
[61] S. Yamashita, S. Ohtsuka, N. Akasaka, S. Ukai, S. Ohnuki, Formation of nanoscale complex oxide particles in mechanically alloyed ferritic steel, Phil. Mag. Lett. 84 (8) (2004) 525–529.
[62] M.K. Miller, K.F. Russell, D.T. Hoelzer, Characterization of precipitates in MA/ODS ferritic alloys, J. Nucl. Mater. 351 (1–3) (2006) 261–268.
[63] J.B. Seol, D. Haley, D.T. Hoelzer, J.H. Kim, Influences of interstitial and extrusion temperature on grain boundary segregation, Y–Ti–O nanofeatures, and mechanical properties of ferritic steels, Acta Mater. 153 (2018) 71–85.
[64] A. Hirata, T. Fujita, Y.R. Wen, J.H. Schneibel, C.T. Liu, M.W. Chen, Atomic structure of nanoclusters in oxide-dispersion-strengthened steels, Nat. Mater. 10 (12) (2011) 922–926.
[65] C.A. Williams, G.D. Smith, E.A. Marquis, Quantifying the composition of yttrium and oxygen rich nanoparticles in oxide dispersion strengthened steels, Ultramicroscopy 125 (2013) 10–17.
[66] C.A. Williams, P. Unifantowicz, N. Baluc, G.D.W. Smith, E.A. Marquis, The formation and evolution of oxide particles in oxide-dispersion-strengthened ferritic steels during processing, Acta Mater. 61 (6) (2013) 2219–2235.
[67] G.R. Odette, Recent progress in developing and qualifying nanostructured ferritic alloys for advanced fission and fusion applications, JOM (J. Occup. Med.) 66 (12) (2014) 2427–2441.
[68] G.R. Odette, On the status and prospects for nanostructured ferritic alloys for nuclear fission and fusion application with emphasis on the underlying science, Scripta Mater. 143 (2018) 142–148.
[69] A.J. London, S. Lozano-Perez, M.P. Moody, S. Amirthapandian, B.K. Panigrahi, C.S. Sundar, C.R. Grovenor, Quantification of oxide particle composition in model oxide dispersion strengthened steel alloys, Ultramicroscopy 159 Pt 2 (2015) 360–367.
[70] E.A. Marquis, Core/shell structures of oxygen-rich nanofeatures in oxide-dispersion strengthened Fe–Cr alloys, Appl. Phys. Lett. 93 (18) (2008).
[71] V. Badjeck, M.G. Walls, L. Chaffron, J. Malaplate, K. March, New insights into the chemical structure of Y 2 Ti 2 O 7−δ nanoparticles in oxide dispersion-strengthened steels designed for sodium fast reactors by electron energy-loss spectroscopy, J. Nucl. Mater. 456 (2015) 292–301.
[72] K. Dawson, S.J. Haigh, G.J. Tatlock, A.R. Jones, Nano-particle precipitation in mechanically alloyed and annealed precursor powders of legacy PM2000 ODS alloy, J. Nucl. Mater. 464 (2015) 200–209.
[73] V.B. Glushkova, V.A. Krzhizhanovskaya, O.N. Egorova, Interactions of yttrium and aluminum oxides, Inorg. Mater. 19 (1) (1983) 80–84.
[74] X. Guo, K. Sakurai, Formation of yttrium aluminum perovskite and yttrium aluminum garnet by mechanical solid-state reaction, Jpn. J. Appl. Phys. 39 (3R) (2000) 1230.